# Supplementary Information

**Programmable high-sensitivity iontronic pressure sensors support broad human-interactive perception and identification**

Yue Huang[1], Shaoxiong Hu[1,2*], Ying Li[1], Rui Wang[1], Yucheng Yang[1], Wei Zhu[1,2*] and Yuan Deng[1,2*]

1 School of Materials Science and Engineering, Beihang University, Beijing 100191, China

2 Key Laboratory of Intelligent Sensing Materials and Chip Integration Technology of Zhejiang Province, Hangzhou Innovation Institute of Beihang University, Hangzhou 310052, China

* Corresponding author. Email: hushaoxiong@buaa.edu.cn; zhu_wei@buaa.edu.cn; dengyuan@buaa.edu.cn

**Supplementary movie** Handwriting recognition and encryption system demonstration

**This PDF file includes:**

**Supplementary Figs. 1 to 25**

**Supplementary Tables 1 to 2**

Supplementary Fig. 1 Photograph of the iontronic pressure sensor.

Supplementary Fig. 2 SEM images and EDS elemental maps for S, F, and N of TPU/DMF and ionogel (40 wt%).

Supplementary Fig. 3 Nyquist plots of the ionogels with varying mass ratios.

Supplementary Fig. 4 Photographs demonstrate the high ionic conductivity of the ionogel.

Supplementary Fig. 5 Cyclic stability of the ionogels with different mass ratios.

Supplementary Fig. 6 Electrochemical performances of an iontronic sensor without spacers under 10 kPa.

Supplementary Fig. 7 Rheological behaviors of TPU and ionogels.

Supplementary Fig. 8 Characterization of planar iontronic pressure sensors.

Supplementary Fig. 9 Performance comparison of the planar iontronic sensor with ionogels of different thickness.

Supplementary Fig. 10 Performance comparison of the iontronic pressure sensors among uniform microstructures.

Supplementary Fig. 11 Illustrations and characterizations of the iontronic pressure sensors with gradient microstructures.

Supplementary Fig. 12 Optical images of TPU with uniform microstructures before and under loading pressure.

Supplementary Fig. 13 Images of gradient microstructures before and under loading pressure.

Supplementary Fig. 14 Capacitive performance of sensor IV.

Supplementary Fig. 15 Long-term stability of sensor IV over ten days.

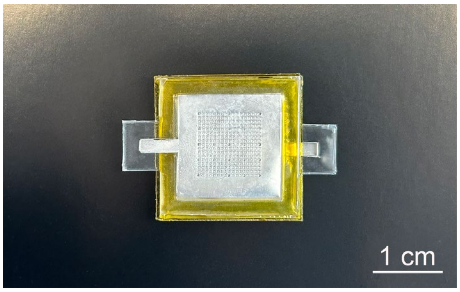


**Supplementary Fig. 1 Photograph of the iontronic pressure sensor.**

The overall size of the sensor with borders is 2.2 cm × 2.2 cm.

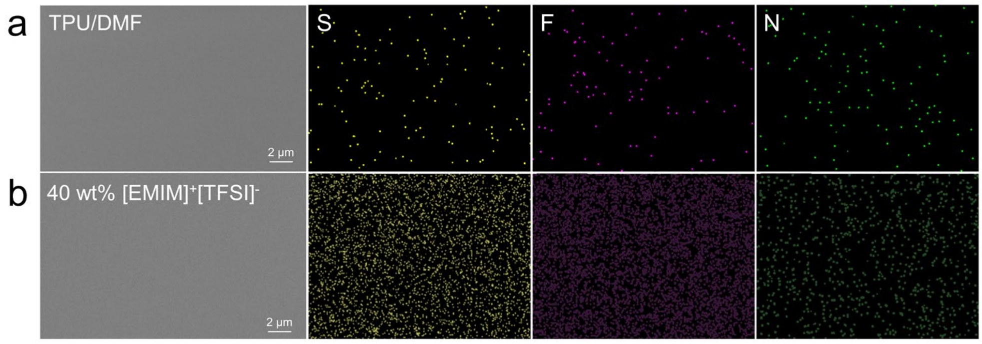


**Supplementary Fig. 2 SEM images and EDS elemental maps for S, F, and N of a** TPU/DMF and **b** ionogel (40 wt%). These results indicate an increased in S, and F elements, primarily originated from $[TFSI]^{-}$. The N element is derived from $[EMIM]^{+}$, $[TFSI]^{-}$, and TPU.

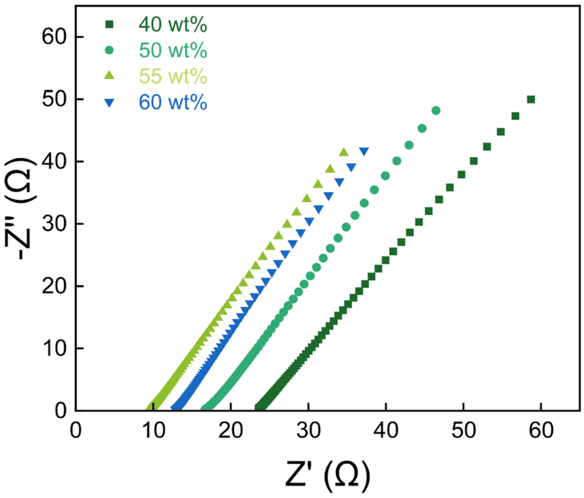


**Supplementary Fig. 3 Nyquist plots of the ionogels with varying mass ratios.** The ionic conductivity of the ionogels is calculated using the equation: $\sigma = \frac{d}{R \cdot S}$, where *d* represents the thickness of the ionogel, *R* is the bulk resistance of the ionogel, and *S* denotes the contact area between the test electrodes and the ionogel. The value of *R* is determined by the intercept with the X-axis in the Nyquist plots.

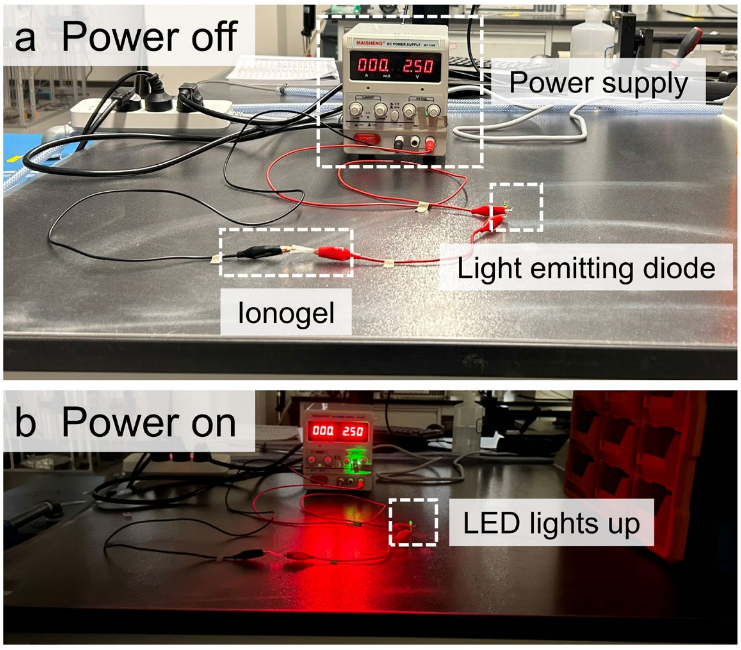


**Supplementary Fig. 4 Photographs demonstrate the high ionic conductivity of the ionogel. a** The ionogel acts as a conductor, connecting a light emitting diode (LED) to a power supply. **b** When the power supply is switched on, the LED lights up.

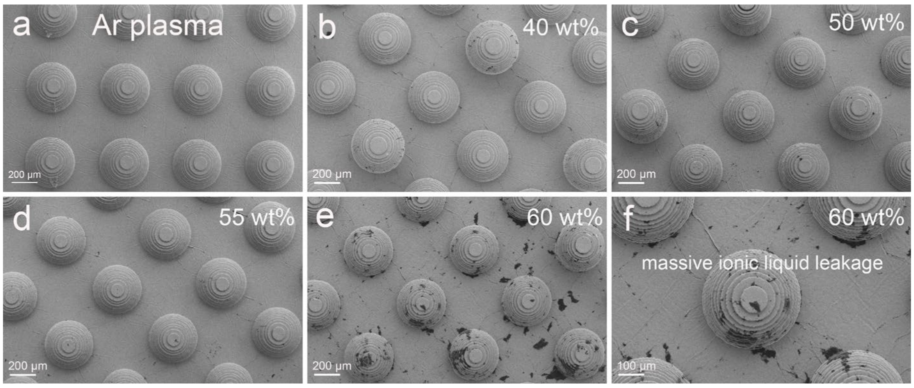


**Supplementary Fig. 5 Cyclic stability of the ionogels with different mass ratios. a** The original microstructural electrode after Ar plasma treatment. Microstructural electrodes were assembled with the ionogels to endure dynamic pressure loading of 700 kPa over 100 cycles. The electrodes were tested with **b** 40 wt%, **c** 50 wt%, **d** 55 wt% and **e** 60 wt% ionogels. **f** An enlarged image of **e** shows massive ionic liquid leakage from the 60 wt% ionogel.

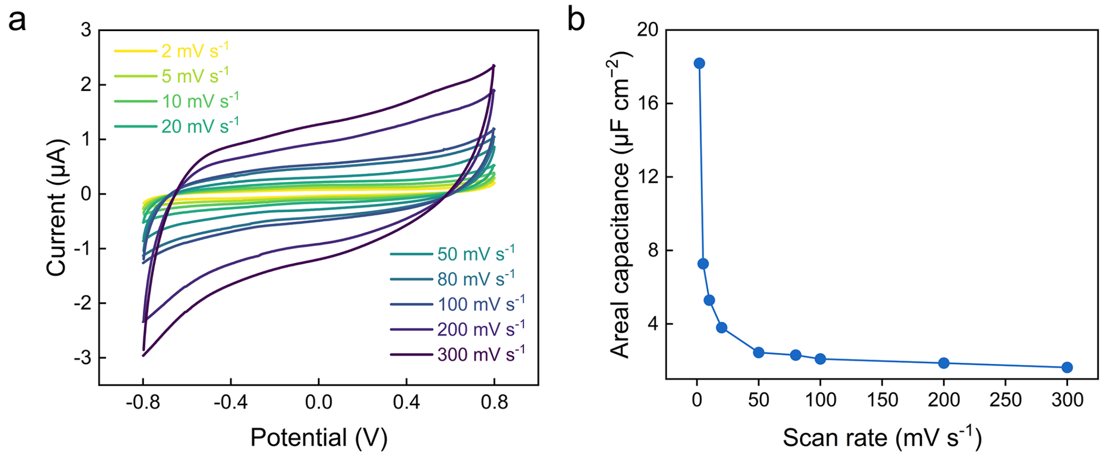


**Supplementary Fig. 6 Electrochemical performances of an iontronic sensor without spacers under 10 kPa. a** CV curves at different scan rates from 1 to 60 mV $s^{-1}$. **b** The areal capacitances at different scan rates.

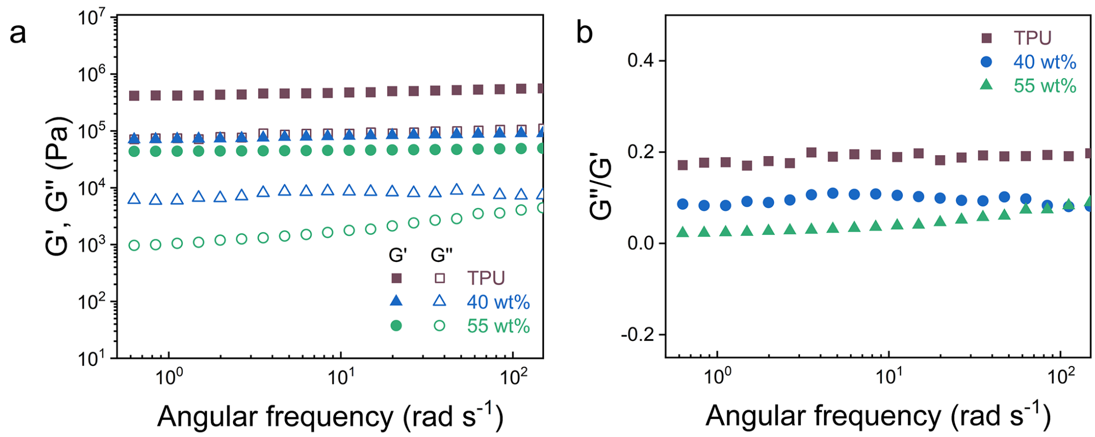


**Supplementary Fig. 7 Rheological behaviors of TPU and ionogels. a** The storage modulus (G') and loss modulus (G'') of TPU and ionogels. **b** G''/G' ratios as a function of frequency for TPU and ionogels.

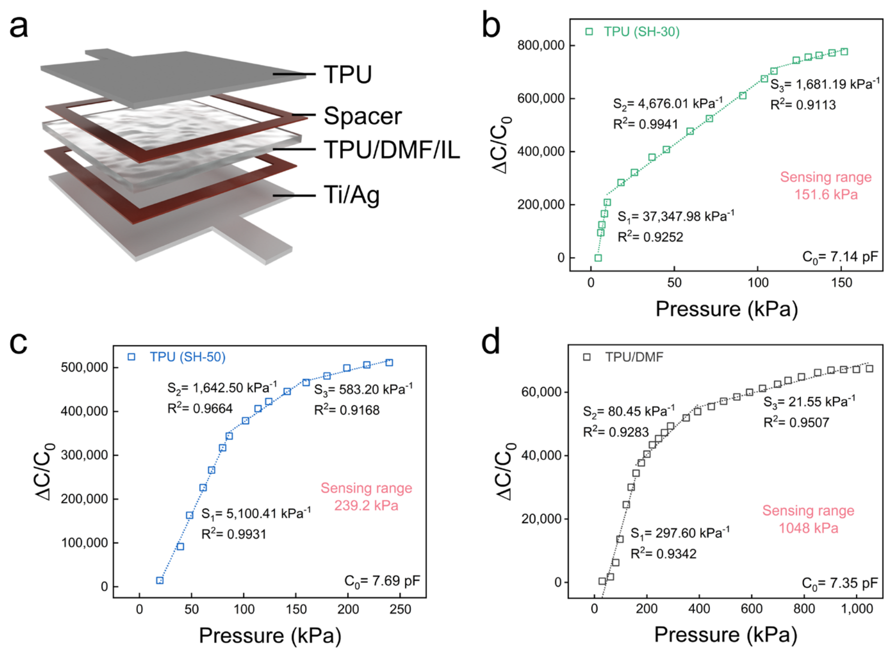


**Supplementary Fig. 8 Characterization of planar iontronic pressure sensors. a** Structure design of the planar sensors. Sensing performance comparison between sensors with different secondary curing TPU: **b** The iontronic pressure sensor based on TPU (SH-30) exhibits notably high sensitivity of 37,347.98 kPa$^{-1}$ within the range from 4.3 kPa to 9.7 kPa ($C_0$ = 7.14 pF). The measured sensitivities are 4,676.01 kPa$^{-1}$ for the 9.7-109.5 kPa range and 1,681.19 kPa$^{-1}$ for the 109.5-151.6 kPa range. **c** The sensing curve of sensor based on TPU (SH-50) can be divided into three regions, 19.4-85.9 kPa, 85.9-159.5 kPa, 159.5-239.2 kPa. The corresponding sensitivities are 5,100.41 kPa$^{-1}$, 1,642.50 kPa$^{-1}$, 583.20 kPa$^{-1}$, with an initial capacitance of 7.69 pF. **d** The measured sensitivities of sensor based on TPU/DMF are 297.6 kPa$^{-1}$ for the 29.6-158.4 kPa range, 80.46 kPa$^{-1}$ for the 2158.4-393.2 kPa range and 21.55 kPa$^{-1}$ for the 393.2-1,048 kPa range, with an initial capacitance of 7.35 pF.

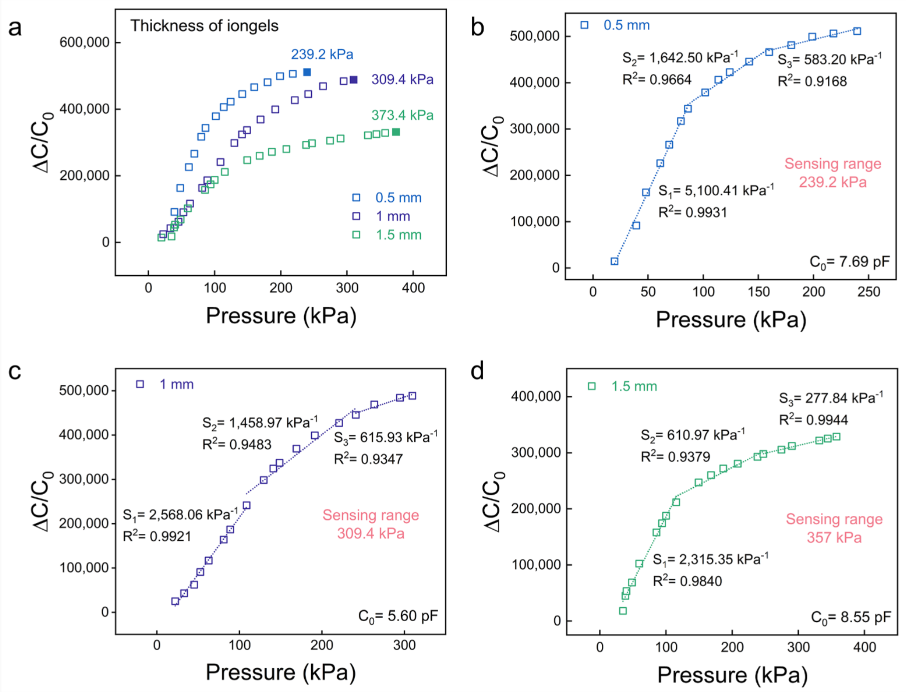


**Supplementary Fig. 9 Performance comparison of the planar iontronic sensor with ionogels of different thickness. a** Sensing performance comparison. **b** The iontronic pressure sensor based on TPU (SH-50) with a 0.5 mm thick ionogel. **c** The sensing curve of sensor based on TPU (SH-50) with a 1 mm thick ionogel, which can be divided into three regions, 22.1-108.6 kPa, 108.6-241 kPa, 241-309.4 kPa. The corresponding sensitivities are 2,568.06 $kPa^{-1}$, 1,458.97 $kPa^{-1}$, 615.93 $kPa^{-1}$, with an initial capacitance of 5.60 pF. **d** The iontronic pressure sensor based on TPU (SH-50) with a 1.5 mm thick ionogel exhibits high sensitivity of 2,315.35 $kPa^{-1}$ within the range from 34.6 kPa to 115.1 kPa ($C_0$ = 8.55 pF). The measured sensitivities are 610.9 $kPa^{-1}$ for the 115.1-246.5 kPa range and 277.84 $kPa^{-1}$ for the 246.5-357 kPa range.

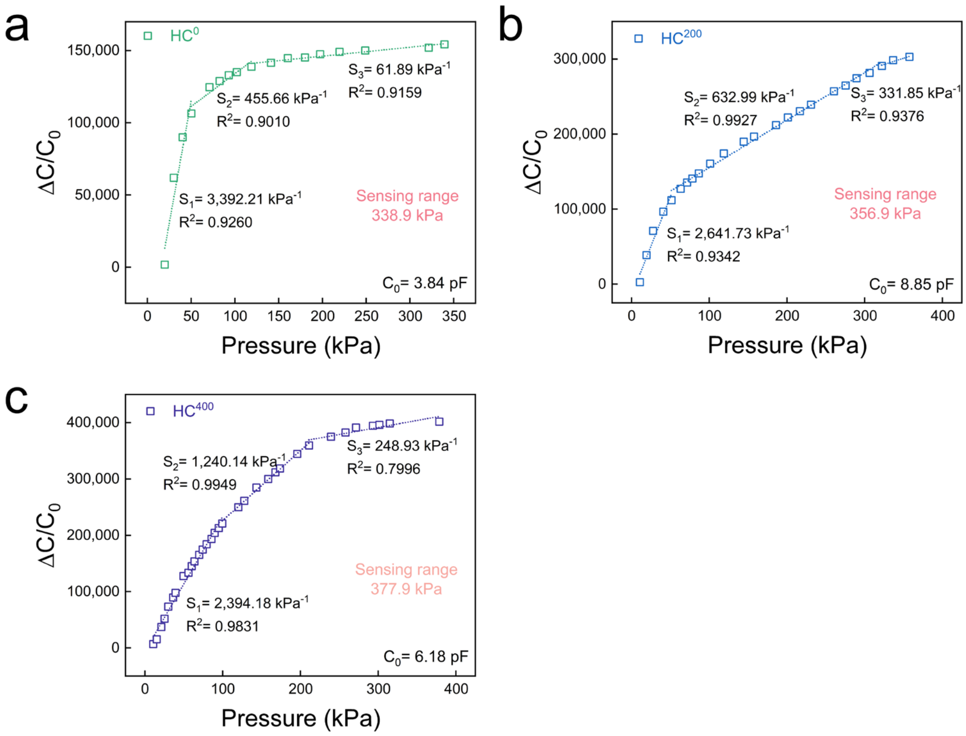


**Supplementary Fig. 10 Performance comparison of the iontronic pressure sensors among uniform microstructures: a** The $HC^0$-based sensor exhibits sensitivities of 3,392.21 $kPa^{-1}$, 266.07 $kPa^{-1}$ and 55.17 $kPa^{-1}$ corresponding to 19.7-50 kPa, 50-118.5 kPa, and 118.5-338.9 kPa range ($C_0$=3.84 pF). **b** The measured sensitivities of $HC^{200}$-based sensor are 2,641.73 $kPa^{-1}$ for the 10.6-51.2 kPa range, 632.98 $kPa^{-1}$ for the 51.2-321.5 kPa range and 331.85 $kPa^{-1}$ for the 321.5-356.9 kPa range, with an initial capacitance of 8.85 pF. **c** The sensing curve of $HC^{200}$-based sensor can be divided into three regions, 10.5-99.2 kPa, 99.2-210.7 kPa, 238.8-377.9 kPa, and corresponds to 2,394.18 $kPa^{-1}$, 1240.14 $kPa^{-1}$, 248.93 $kPa^{-1}$, with an initial capacitance of 6.18 pF.

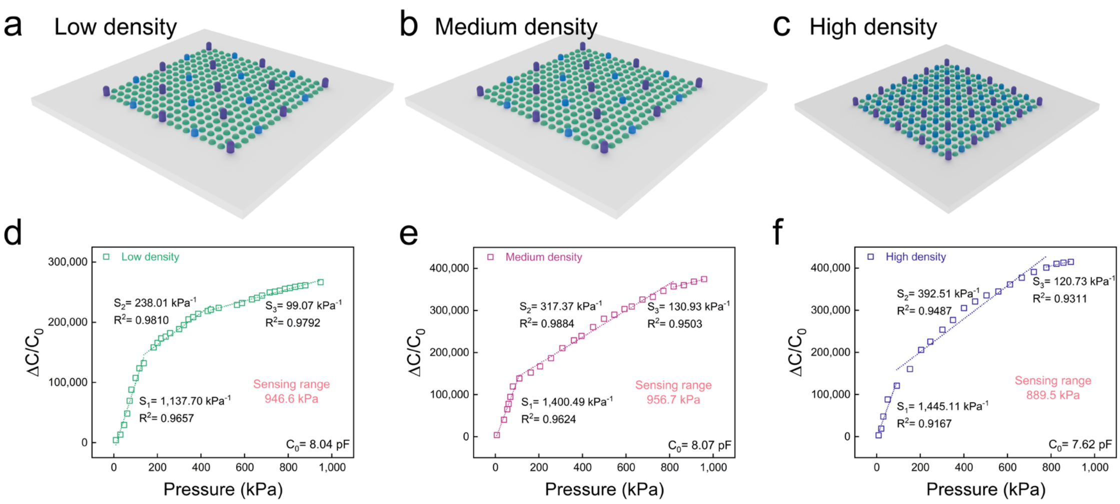


g

| Density | Microstructure number | | | |
|---|---|---|---|---|
| | $HC^0$ | $HC^{200}$ | $HC^{400}$ | Total |
| Low | 266 | 14 | 9 | 289 |
| Medium | 264 | 12 | 13 | 289 |
| High | 208 | 56 | 25 | 289 |

**Supplementary Fig. 11 Illustrations and characterizations of the iontronic pressure sensors with gradient microstructures.** Microstructure array demonstrations of **a** Low density, **b** Medium density, and **c** High density. **d** The low density sensor exhibits sensitivities of 1,137.70 kPa$^{-1}$, 265.10 kPa$^{-1}$ and 98.21 kPa$^{-1}$ corresponding to 9.2-136.9 kPa, 136.9-444.1 kPa, and 444.1-946.6 kPa range ($C_0$=8.04 pF). **e** The sensing curve of medium density sensor can be divided into three regions, 6.2-109.7 kPa, 109.7-817 kPa, 817-956.7 kPa, and corresponds to 1,400.49 kPa$^{-1}$, 317.37 kPa$^{-1}$, 130.9 kPa$^{-1}$, with an initial capacitance of 8.07 pF. **f** The measured sensitivities of high density sensor are 1,445.11 kPa$^{-1}$ for the 8.5-91.6 kPa range, 392.51 kPa$^{-1}$ for the 91.6-776.7 kPa range and 120.73 kPa$^{-1}$ for the 776.7-889.5 kPa range, with an initial capacitance of 7.62 pF. **g** Detailed microstructure counts for the three densities.

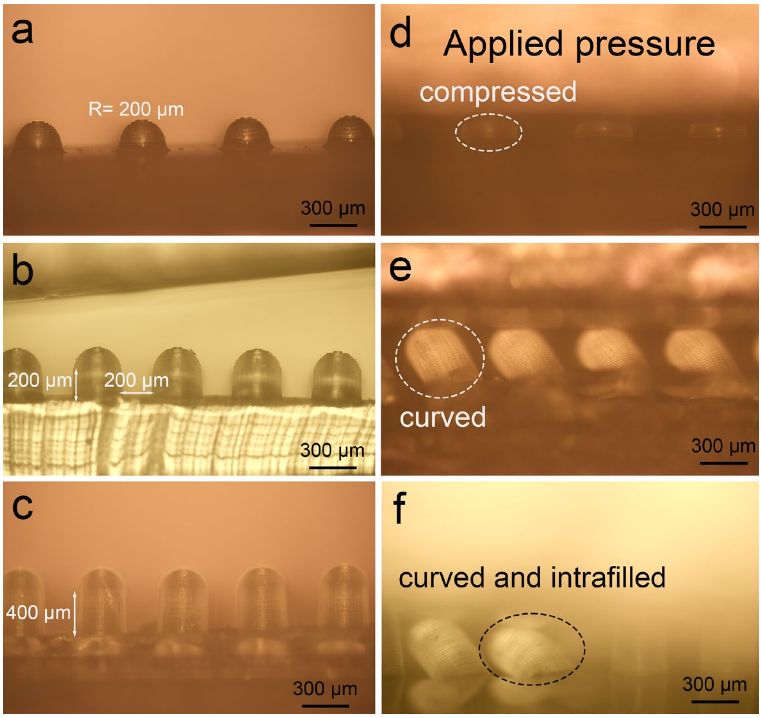


**Supplementary Fig. 12 Optical images of TPU with uniform microstructures before and under loading pressure.** Original status of **a** $HC^{0}$, **b** $HC^{200}$, and **c** $HC^{400}$, respectively. When these microstructures come into contact with a flat surface of ionogels, **d** $HC^{0}$, **e** $HC^{200}$, and **f** $HC^{400}$ exhibit different deformations under pressure.

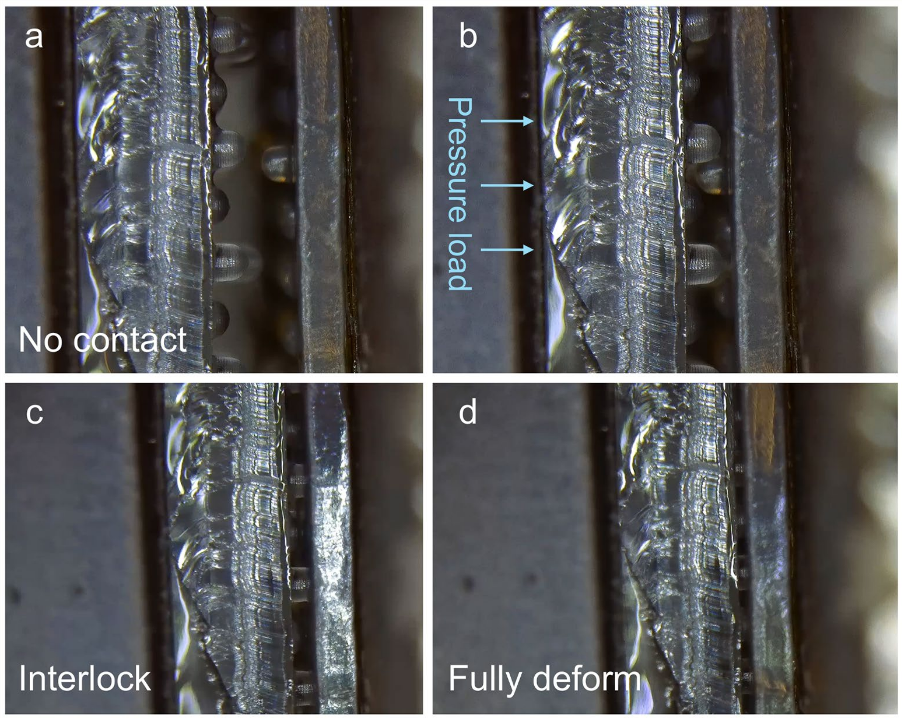


**Supplementary Fig. 13 Images of gradient microstructures before and under loading pressure. a** Original status. **b-d** Microstructural changes with increasing pressure load. Progressive deformation occurs as pressure increases, leading to visible structural compression.

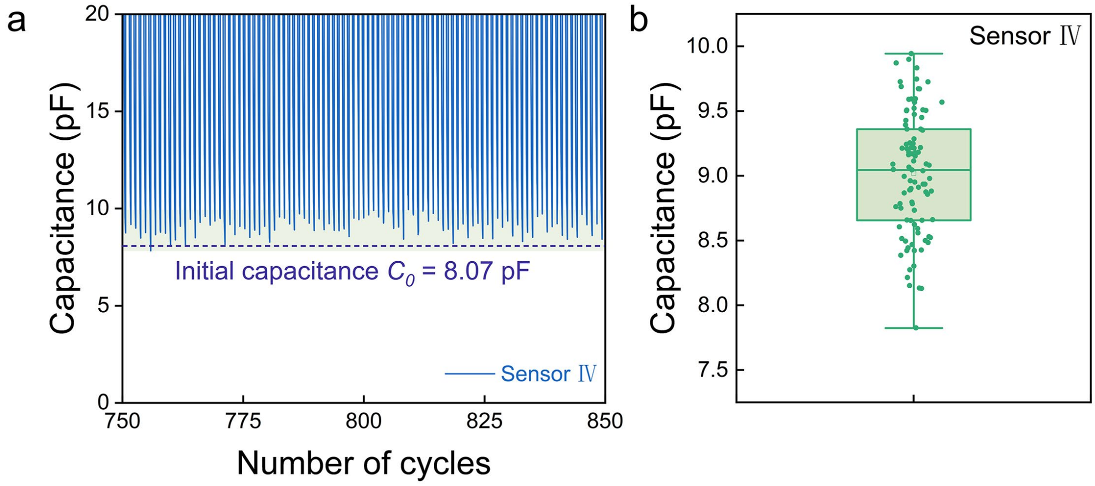


**Supplementary Fig. 14 Capacitive performance of sensor IV. a** The final capacitances in 100 cycles of the stability test. **b** Boxplot of the final capacitances and average final capacitance of sensor IV is 9.02 pF.

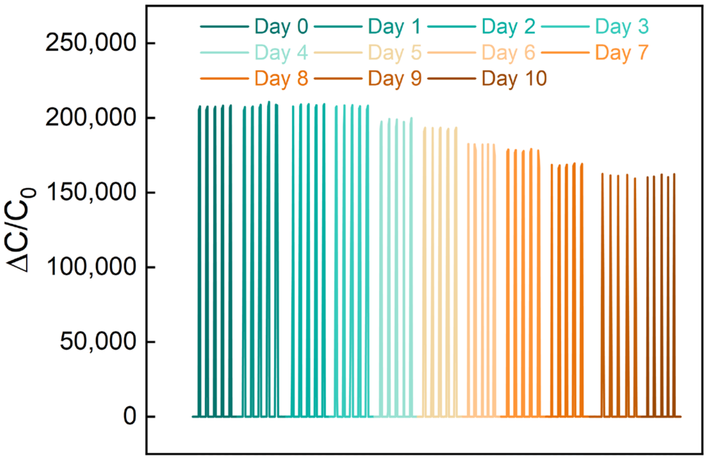


**Supplementary Fig. 15 Long-term stability of sensor IV over ten days.** Dynamic capacitive response to a cycling pressure of 300 kPa within ten days.

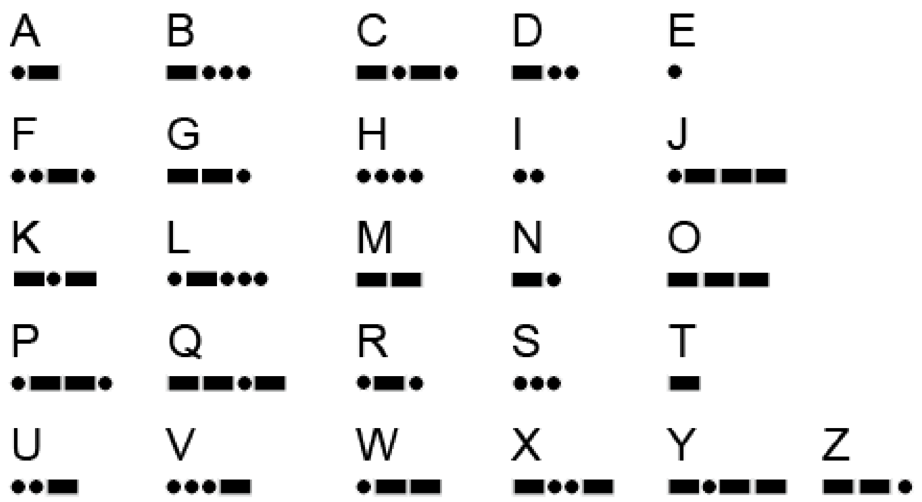


**Supplementary Fig. 16 Morse code for the 26 letters from A to Z.** The pressure sensor is utilized to transmit Morse code information.

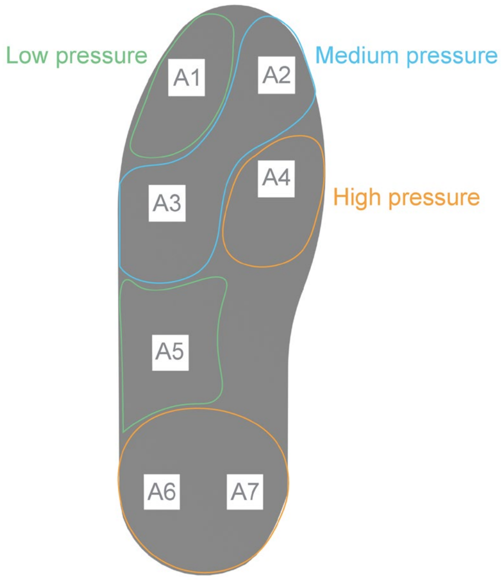


**Supplementary Fig. 17 Plantar pressure zone according to the physiological divisions of medical anatomy.** The pressure on the toe 2-5 is assessed by A1, and the pressure on the midfoot is evaluated by A5, which sustain low pressure. Medium pressures on toe 1, and meta 3-5 are measured by A2, and A3, respectively. The meta 1-2, heel lateral, and heel medial withstand high pressure, characterized by A4, A6, and A7, respectively.

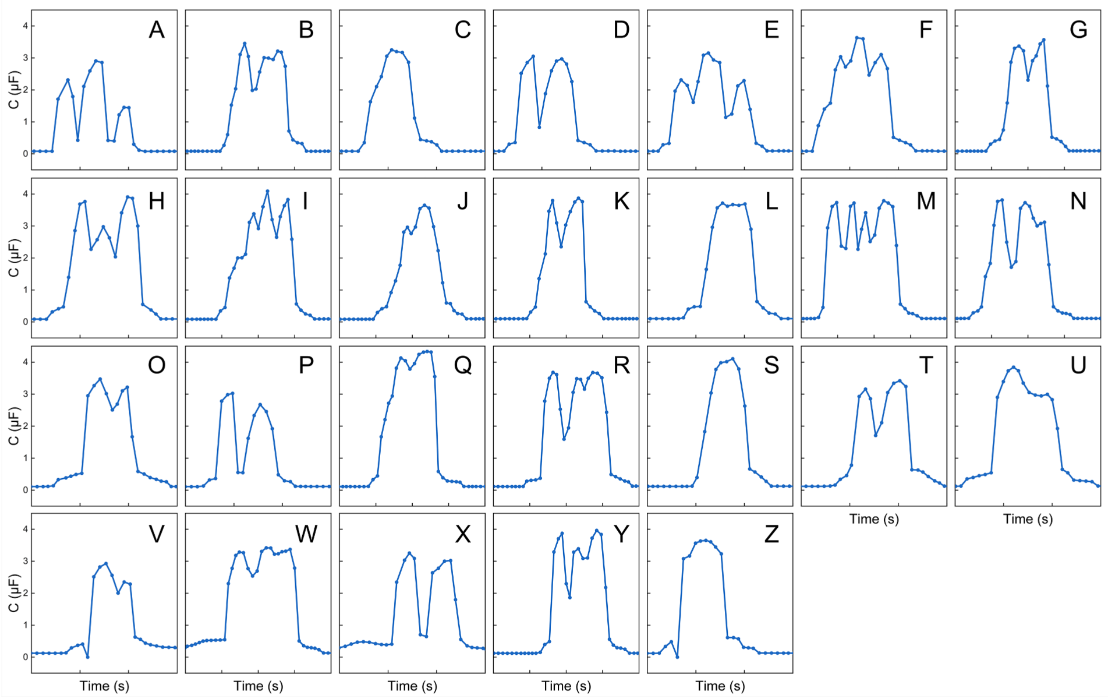


**Supplementary Fig. 18 Capacitance curves of 26 English letters handwritten by one volunteer.** The Minimum scale value of the horizontal coordinate time is 1 second. The number of strokes in each letter corresponds to the number of signal peaks; for instance, both "A" and "H" display three peaks. Additionally, stroke length is positively correlated with peak amplitude. In "A," the first two peaks are significantly higher than the third, whereas in "H," the second peak is notably lower. Moreover, letters involving directional changes, such as 'U' or 'V,' exhibit two distinct peaks. This occurs because during the vertical motion of the pen in strokes like "|" or "\," the index finger exerts increasing pressure on the sensor. Conversely, during horizontal or diagonal strokes like "—" or "/," the thumb initiates a slight decrease in sensor pressure, which subsequently increases as the stroke progresses.

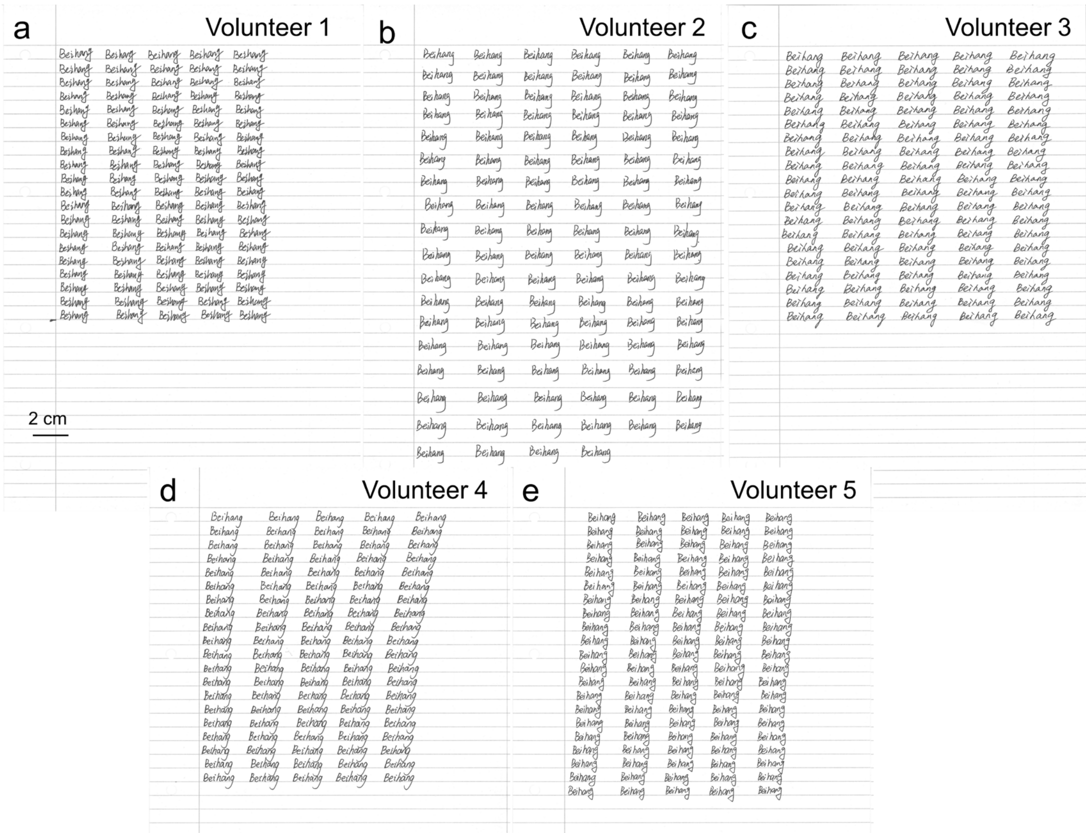


**Supplementary Fig. 19 Example handwriting images by five volunteers of "Beihang".**

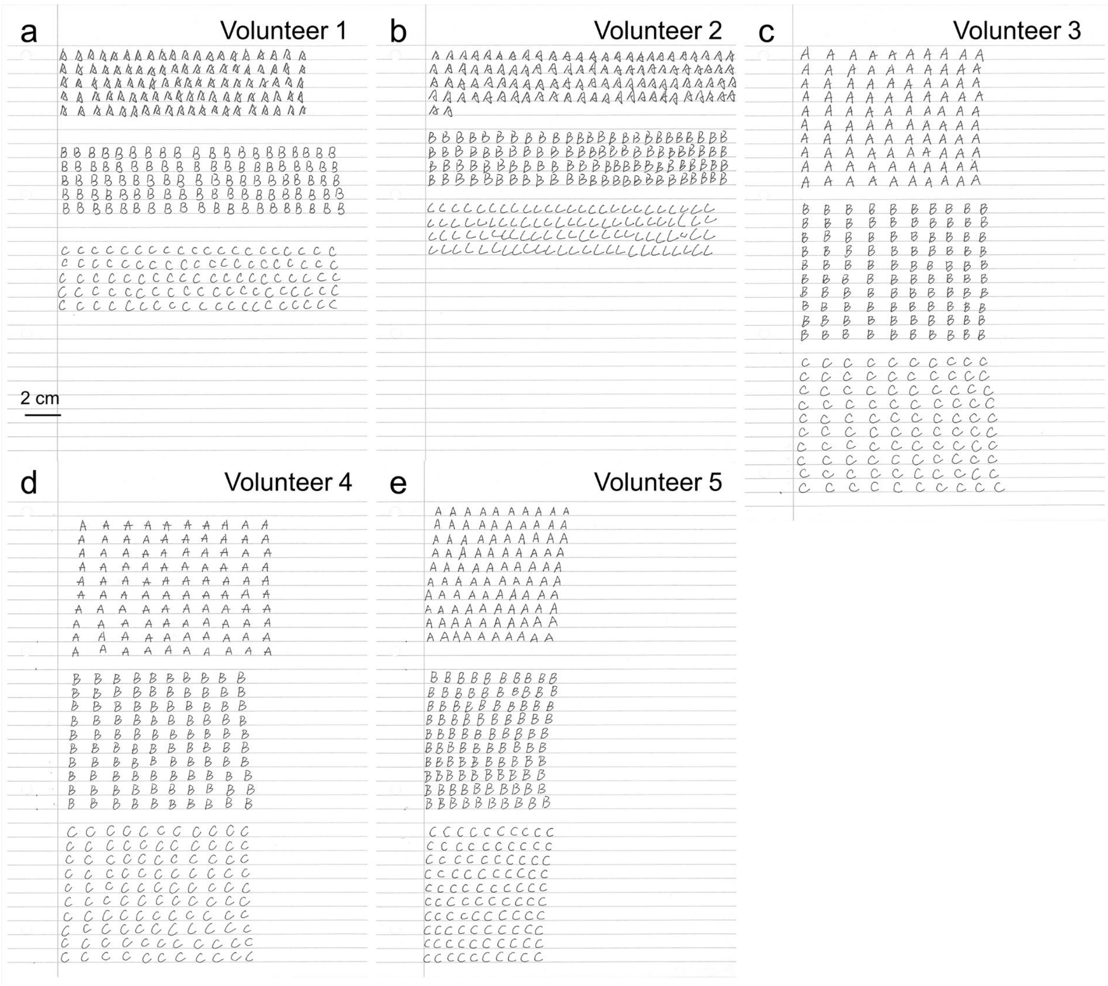


**Supplementary Fig. 20 Example handwriting images by five volunteers of "A," "B" and "C".**

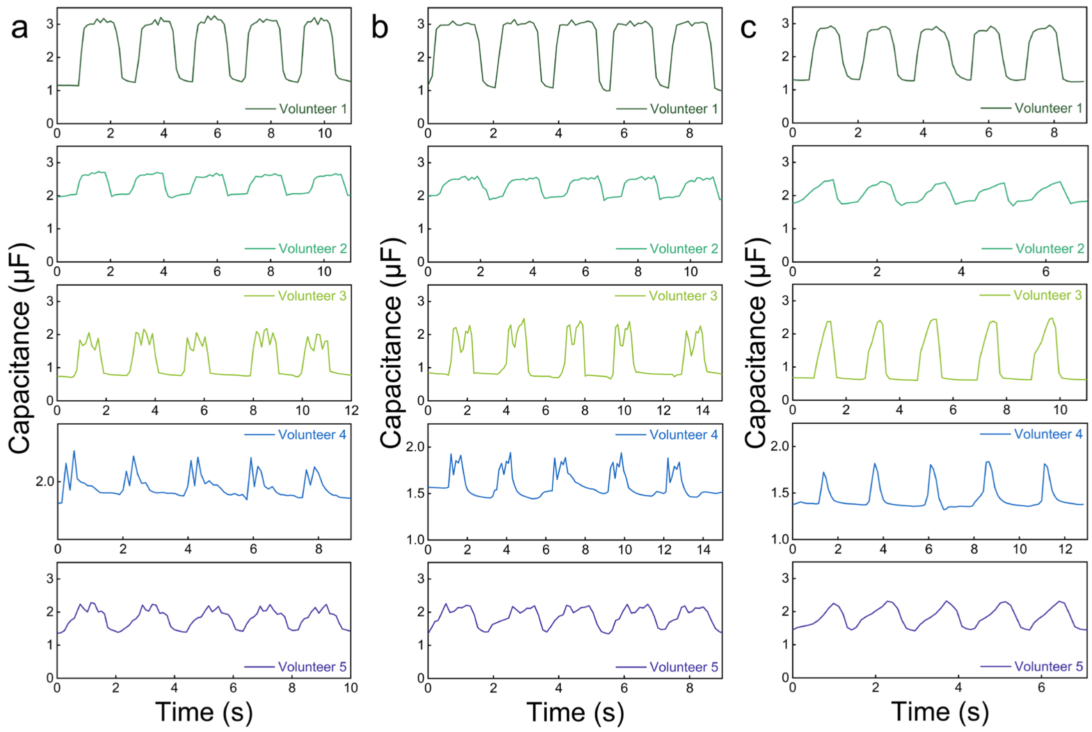


**Supplementary Fig. 21 Capacitive signals from handwriting obtained by five volunteers corresponding to a** "A", **b** "B", and **c** "C".

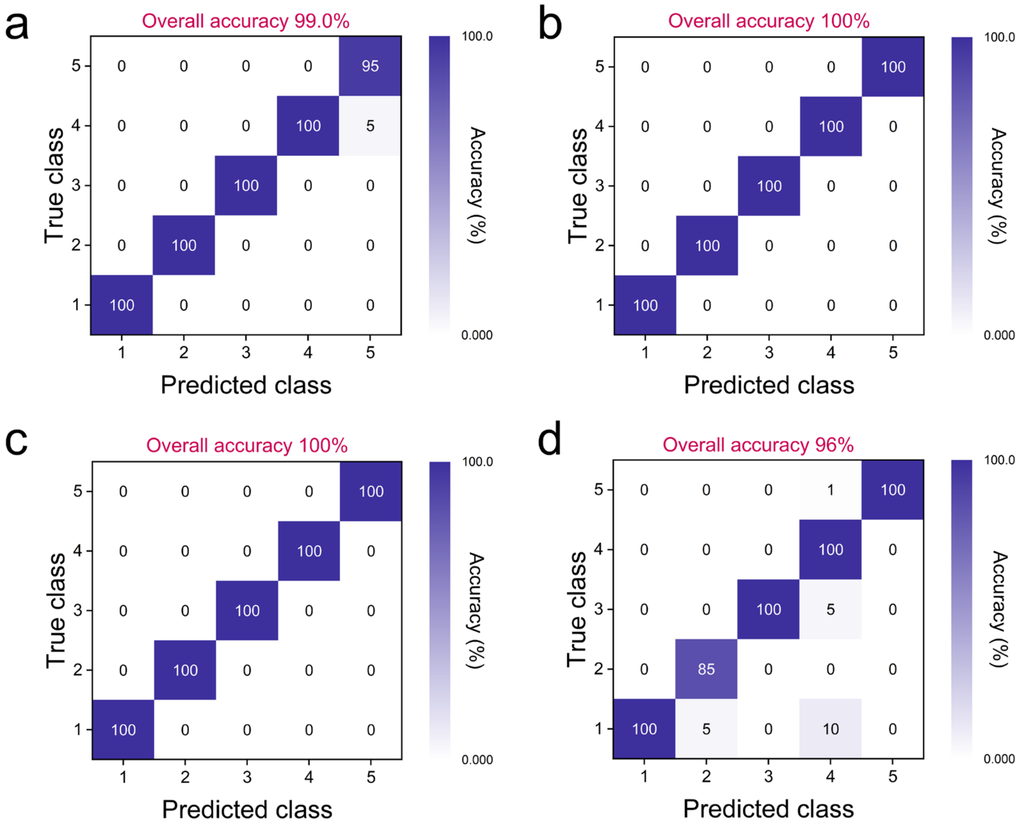


**Supplementary Fig. 22 Model performance.** Confusion matrices displaying the classification accuracy for handwritings by five volunteers: **a** "Beihang", **b** "A", **c** "B" and **d** "C".

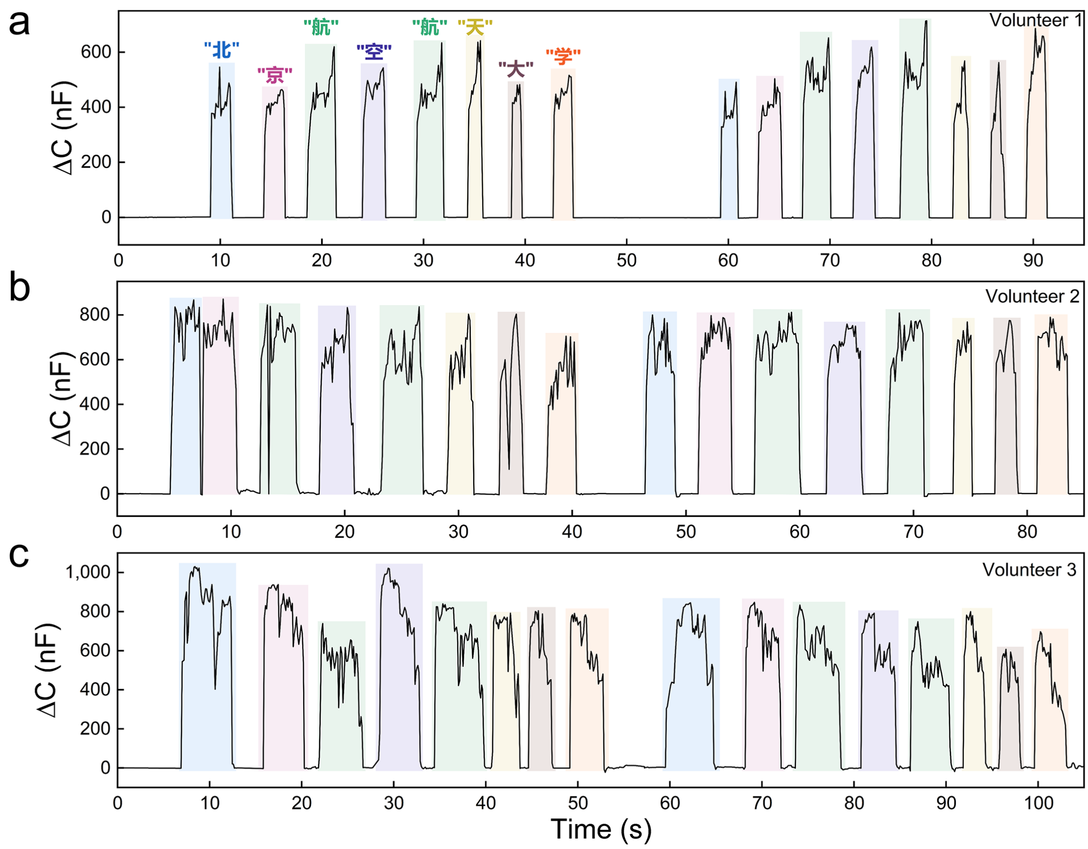


**Supplementary Fig. 23 The real-time capacitance curves recorded during the handwriting of the Chinese characters "北京航空航天大学" (meaning "Beihang University") by three volunteers.** Within a single handwriting session by the same volunteer, the shapes of the capacitance signal peaks vary across different Chinese characters but remain consistent for identical Chinese characters. The peak shapes of the same Chinese character differ between volunteers, with peak values of 600 nF, 800 nF, and 1000 nF, respectively, reflecting variations in grip pressure during writing.

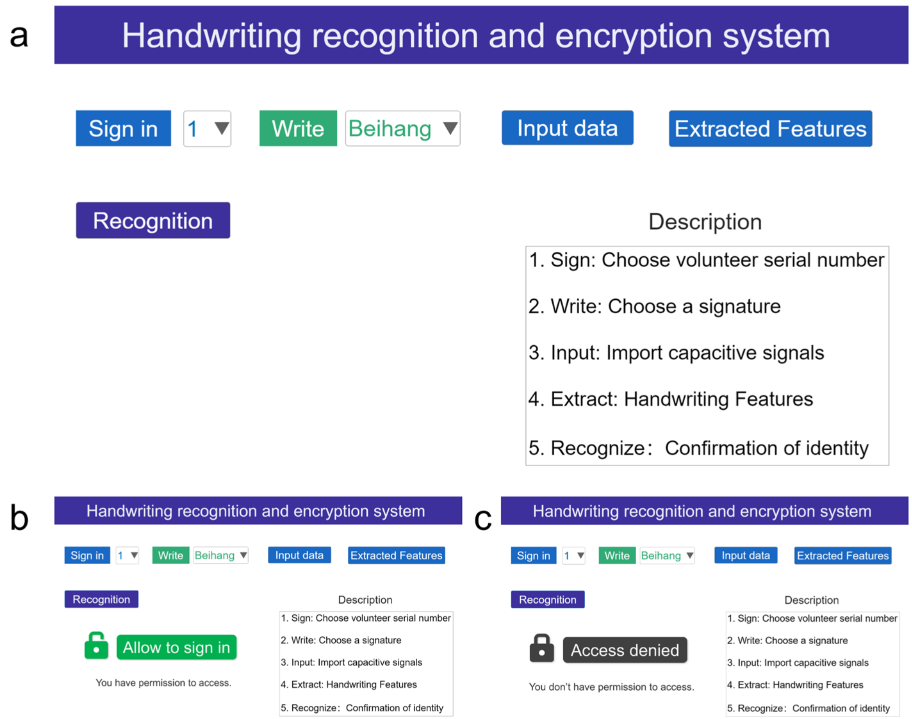


**Supplementary Fig. 24 User-interactive display for handwriting recognition and encryption in Matlab. a** The user interface**. b** Successful authentication of secure access. **c** Unsuccessful authentication attempt.

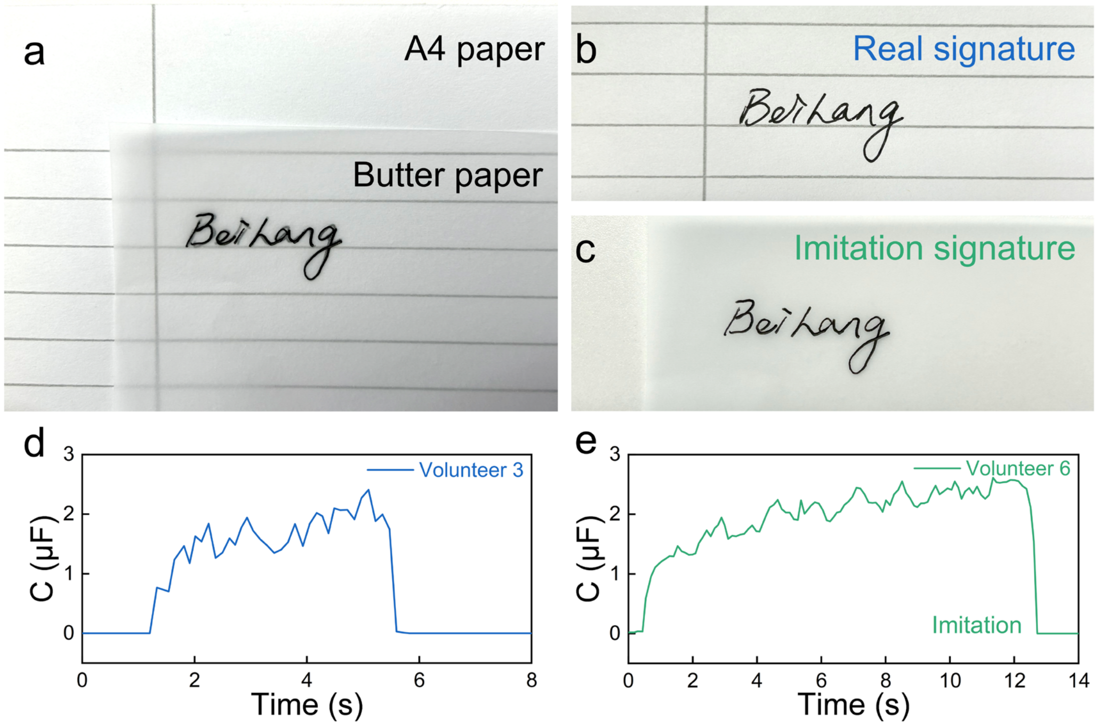


**Supplementary Fig. 25 Verification of signature authenticity. a** Image showing the imitation of the "Beihang" signature using butter paper. **b** Image of the authentic signature. **c** Image of the imitated signature. **d** Capacitive signals corresponding to the authentic signature by Volunteer 3. **e** Capacitance curve of the imitated signature by Volunteer 6.

**Supplementary Table 1 Comparison of the fabrication, reliability and stability of iontronic pressure sensors.**

| Sensing material | Fabrication | Reliability and Stability | Sensing range |
|---|---|---|---|
| Iontronic nanofibrous membrane[1] | Electrospun | 4,000 cycles (10 kPa) | 30 kPa |
| Iontronic nanofibrous membrane[2] | Electrospun | 10,000 cycles (150 kPa) | 700 kPa |
| Iontronic hollow-porous fiber[3] | Solvent exchange | 3,500 cycles (10 kPa) | 600 kPa |
| Iontronic fiber[4] | Solution blow-spinning | 10,000 cycles (1,970 kPa) | 4 MPa |
| Iontronic fibric[5] | Dip coating | 5,500 cycles (150 kPa) | 150 kPa |
| Ionogel[6] | Solution casting | 5,000 cycles (300 kPa) | 360 kPa |
| Ionogel[7] | Dip coating | 5,000 bending/release cycles (bending radius ≈6.1 mm) | 120 kPa |
| Ionogel[8] | Inkjet printing or screen printing | 1,000 cycles (10 kPa) | 25 kPa |
| Ionogel[9] | In-situ UV polymerization | 1,500 cycles (177 kPa) | 330 kPa |
| Heterophasic ionogels[10] | In-situ UV polymerization | 2,000 cycles (50 kPa) | 200 kPa |
| Nanostructured ionogel[11] | UV polymerization | 2,000 cycles (14 kPa) | 100 kPa |
| Porous ionogel[12] | Freeze-drying method | 10,000 cycles (20 kPa) | 106 kPa |
| Porous ionogel[13] | Sacrificial template and solution immersion | 11,800 cycles (12.5 kPa) | 400 kPa |
| Ionogel (This work) | Solution casting | 1,500 cycles (100 kPa) | 151.6 kPa |
| | | 1,500 cycles (900 kPa) | 956.7 kPa |

**Supplementary Table 2 Performance comparison of this work with reported works.**

| Mechanism | Sensing material | Microstructure | Sensing range (kPa) | Sensitivity ($kPa^{-1}$) |
|---|---|---|---|---|
| Iontronic[14] | TPU/[EMIm][$NTf_2$] | Cup-shaped microcolumn | 170 | 87.75 (0-0.5 kPa)<br>19.51 (0.5-25 kPa)<br>4.80 (25-60 kPa)<br>1.37 (60-170 kPa) |
| Iontronic[6] | PVA/$H_3PO_4$ | Graded intrafillable microstructures | 360 | 3302.9 (0-10 kPa)<br>671.7 (10-100 kPa)<br>229.9 (100-360 kPa) |
| Iontronic[3] | TPU/DMA/[HMIM][$BF_4$] | Hollow-porous fiber | 600 | 7.26 (0-12 kPa)<br>1.35 (12-71 kPa)<br>0.49 (71-600 kPa) |
| Capacitive[15] | Ag/PDMS | Flea leg-like 3D cellular structures | 200 | 1.005 (0-1 kPa)<br>0.625 (1-100 kPa)<br>0.082 (100-200 kPa) |
| Capacitive[16] | PDMS | Octopus sucker | 500 | 0.106 (1-60 kPa)<br>0.0135 (60-500 kPa) |
| Capacitive[17] | P(VDF-TrFE)/$TiO_2$/PVA/Ag | Cocklebur-inspired | 200 | 0.163 (0-20 kPa)<br>0.027 (20-200 kPa) |
| Resistive[18] | Reduced graphene oxide | Micro cone | 300 | 133.003 (0-40 kPa)<br>34.423 (40-100 kPa) |

| | | | | |
|---|---|---|---|---|
| | | | | 11.369 (100-300 kPa) |
| Resistive[19] | CNT/PDMS | Mushroom-mimetic | 150 | 138 (0-10 kPa) 600 (10-20 kPa) 131 (20-50 kPa) 16 (50-150 kPa) |
| Resistive[20] | CNT/PDMS | Gradient pore/pyramid | 1000 | 40.12 (0-1 MPa) |
| Piezoelectric[21] | Fluorinated ethylene propylene (FEP)/Eco-flex/FEP | Microhole | 22.5 | 32.5 nA $kPa^{-1}$ (0.125-5.25 kPa), 6.71 nA $kPa^{-1}$ (7.50-22.5 kPa) |
| Piezoelectric[22] | ZnO | Nanorod | 1000 | 0.403 mV $kPa^{-1}$ (0-1 MPa) |
| Piezoelectric[23] | Wood sponge | Porous | 22.2 | 37.8 mV $kPa^{-1}$ |
| Triboelectric[24] | P(VDF-TrFE)/PDMS | Interlocked microridges | 100 | 550 mV $kPa^{-1}$ (0-20 kPa), 200 mV $kPa^{-1}$ (20-100 kPa) |
| Triboelectric[25] | CNT/cellulose | Bamboo-like | 19.6 | 33.61 (0-2.25 kPa) 4.92 (2.25-19.6 kPa) |
| Triboelectric[26] | AgNWs/PDMS | Zebrine leaf cone patterns | 50 | 127.22 mV $kPa^{-1}$ (0-50 kPa) |

## References

1. Lin X, Xue H, Li F, Mei H, Zhao H & Zhang T. All-nanofibrous ionic capacitive pressure sensor for wearable applications. *ACS Appl Mater Interfaces* **14**, 31385-31395 (2022).

2. Sharma S, et al. Graphene-polymer nanocomposites electrode with ionic nanofibrous membrane for highly sensitive supercapacitive pressure sensor. *Nano Today* **48**, 101698 (2023).

3. Feng Z, et al. Iontronic textile-based capacitive pressure sensor for unconstrained respiration and heartbeat monitoring. *Adv Mater Technol* **8**, 2300949 (2023).

4. Li W, et al. Integrated fibrous iontronic pressure sensors with high sensitivity and reliability for human plantar pressure and gait analysis. *ACS Nano* **18**, 14672-14684 (2024).

5. Wang Q, et al. Finger–coding intelligent human–machine interaction system based on all–fabric ionic capacitive pressure sensors. *Nano Energy* **116**, 108783 (2023).

6. Bai N, et al. Graded intrafillable architecture-based iontronic pressure sensor with ultra-broad-range high sensitivity. *Nat Commun* **11**, 209 (2020).

7. Liu Q, et al. Highly transparent and flexible iontronic pressure sensors based on an opaque to transparent transition. *Adv Sci* **7**, 2000348 (2020).

8. Li S, et al. All-in-one iontronic sensing paper. *Adv Funct Mater* **29**, 1807343 (2019).

9. Shen Z, Zhu X, Majidi C & Gu G. Cutaneous ionogel mechanoreceptors for soft machines, physiological sensing, and amputee prostheses. *Adv Mater* **33**, 2102069 (2021).

10. Zhuo S, Song C, Rong Q, Zhao T & Liu M. Shape and stiffness memory ionogels with programmable pressure-resistance response. *Nat Commun* **13**, 1743 (2022).

11. He X, et al. Highly conductive and stretchable nanostructured ionogels for 3d printing capacitive sensors with superior performance. *Nat Commun* **15**, 6431 (2024).

12. Wang P, Cao J, Li Y, Sun G, Shao H & Meng C. Highly breathable and sensitive iontronic wearable sensor based on porous ionic electrolyte and microstructure

for human movement sensing. *Chem Eng J* **495**, 153525 (2024).

13. Wang HL, et al. A dual-responsive artificial skin for tactile and touchless interfaces. *Small* **19**, 2206830 (2023).
14. Li L, Zhu G, Wang J, Chen J, Zhao G & Zhu Y. A flexible and ultrasensitive interfacial iontronic multisensory sensor with an array of unique "cup-shaped" microcolumns for detecting pressure and temperature. *Nano Energy* **105**, 108012 (2023).
15. Guo X, et al. Biologically emulated flexible sensors with high sensitivity and low hysteresis: Toward electronic skin to a sense of touch. *Small* **18**, 2203044 (2022).
16. Guo XH, et al. Highly sensitive and wide-range flexible bionic tactile sensors inspired by the octopus sucker structure. *ACS Appl Nano Mater* **5**, 11028-11036 (2022).
17. Niu H, et al. Cocklebur-inspired "branch-seed-spininess" 3d hierarchical structure bionic electronic skin for intelligent perception. *Nano Energy* **107**, 108144 (2023).
18. Zhang Y, et al. Superior performances via designed multiple embossments within interfaces for flexible pressure sensors. *Chem Eng J* **454**, 139990 (2023).
19. Zhang Y, et al. Mushroom-mimetic 3d hierarchical architecture-based e-skin with high sensitivity and a wide sensing range for intelligent perception. *Mater Horiz* **10**, 5666-5676 (2023).
20. Wang S, et al. High sensitivity tactile sensors with ultrabroad linear range based on gradient hybrid structure for gesture recognition and precise grasping. *Chem Eng J* **457**, 141136 (2023).
21. Chu Y, et al. Human pulse diagnosis for medical assessments using a wearable piezoelectret sensing system. *Adv Funct Mater* **28**, 1803413 (2018).
22. Deng W, et al. A flexible field-limited ordered ZnO nanorod-based self-powered tactile sensor array for electronic skin. *Nanoscale* **8**, 16302-16306 (2016).
23. Sun J, et al. Sustainable and biodegradable wood sponge piezoelectric

nanogenerator for sensing and energy harvesting applications. *ACS Nano* **14**, 14665-14674 (2020).

24. Ha M, et al. Skin-inspired hierarchical polymer architectures with gradient stiffness for spacer-free, ultrathin, and highly sensitive triboelectric sensors. *ACS Nano* **12**, 3964-3974 (2018).
25. Li X, et al. Lightweight and strong cellulosic triboelectric materials enabled by cell wall nanoengineering. *Nano Lett* **24**, 3273-3281 (2024).
26. Yao G, et al. Bioinspired triboelectric nanogenerators as self-powered electronic skin for robotic tactile sensing. *Adv Funct Mater* **30**, 1907312 (2020).